Electronic structure of chromium trihalides beyond density functional theory

Swagata Acharya, Dimitar Pashov, Brian Cunningham, Alexander N. Rudenko, Malte Rösner, Myrta Grüning, Mark van Schilfgaarde, and Mikhail I. Katsnelson

Phys. Rev. B **104**, 155109 — Published 5 October 2021

DOI: 10.1103/PhysRevB.104.155109

Electronic Structure of Chromium Trihalides beyond Density Functional Theory

Swagata Acharya,[1,*] Dimitar Pashov,[2] Brian Cunningham,[3] Alexander N. Rudenko,[1]
Malte Rösner,[1] Myrta Grüning,[4] Mark van Schilfgaarde,[2,5] and Mikhail I. Katsnelson[1]

[1] *Institute for Molecules and Materials, Radboud University, NL-6525 AJ Nijmegen, The Netherlands*
[2] *King's College London, Theory and Simulation of Condensed Matter, The Strand, WC2R 2LS London, UK*
[3] *Centre for Theoretical Atomic, Molecular and Optical Physics, Queen's University Belfast, Belfast BT71NN, Northern Ireland, United Kingdom*
[4] *Atomistic Simulation Centre, Queen's University Belfast, Belfast BT71NN, Northern Ireland, United Kingdom*
[5] *National Renewable Energy Laboratory, Golden, CO 80401, USA*

We explore the electronic band structure of free standing monolayers of chromium trihalides, CrX_3, X= Cl, Br, I, within an advanced *ab-initio* theoretical approach based in the use of Green's function functionals. We compare the local density approximation with the quasi-particle self-consistent GW approximation (QSGW) and its self-consistent extension (QS$G\widehat{W}$) by solving the particle-hole ladder Bethe-Salpeter equations to improve the effective interaction W. We show that at all levels of theory, the valence band consistently changes shape in the sequence ClBrI, and the valence band maximum shifts from the M point to the Γ point. By analysing the dynamic and momentum dependent self energy we show that QS$G\widehat{W}$ adds to the localization of the systems in comparison to QSGW thereby leading to a narrower band and reduced amount of halogens in the valence band manifold. Further analysis shows that X=Cl is most strongly correlated and X=I is least correlated (most 'band-like') as the hybridization between Cr-d and X-p enhances in the direction ClBrI. For $CrBr_3$ and CrI_3 we observe remarkable differences between the QSGW and QS$G\widehat{W}$ valence band structures, while their eigenfunctions are very similar. We show that weak perturbations, like moderate strain, weak changes to the d-p hybridization, and adding small U, can flip the valence band structures between these two solutions in these materials.

With the discovery of ferromagnetic order in CrI_3, the family of chromium trihalides CrX_3, X=Cl, Br, I, has emerged as a new class of magnetic 2D crystals. Ferromagnetism (FM) in a monolayer CrI_3 was first reported in 2017,[1,2] which was followed by observation of FM in $CrBr_3$,[3,4] $CrCl_3$[5] and many other compounds.[6–10] FM is intrinsic to these system, which distinguishes them from traditional 2D *sp*-electron magnets where magnetism is induced by proximity to a FM substrate. Long range-order is typically suppressed in two-dimensional magnets,[11] but it can be stabilized by magneto-crystalline anisotropy, which opens an energy gap in the magnon spectra and therefore protects the FM in two dimensions.[12,13] Due to their layered structure and their weak inter-layer van-der-Waals interactions these systems are loosely coupled to their substrates, which provides greater flexibility in functionalizing them and controlling their properties, e.g. by varying the layer-number or by applying a gate voltage. This offers new possibilities to make spintronic devices with high accuracy and efficiency.[2,14–22]

CrX_3 is a two-dimensional FM insulator with FM originating from the Cr-X-Cr superexchange interaction.[13,23–25] Six Cr^{3+} ions form a honeycomb structure with D_{3d} point group symmetry and each Cr is surrounded by six X in an octahedral geometry (see Fig. 1). The edge-sharing geometry leads to first neighbor Cr atoms sharing a pair of ligands. This enables pathways for Cr-X-Cr super-exchange. In this crystal field geometry, the Cr d splits into a t_{2g} triplet and an e_g doublet. Cr^{3+} has a valence of three electrons, which fill the t_{2g} majority-spin band according to Hund's first rule, leaving all other d bands empty. The ionic model leads to the magnetic moment on each Cr^{3+} ion of $\sim 3\mu_B$ which is confirmed by ab-initio calculations. All three CrX_3 compounds have FM order down to the monolayer with Curie temperatures $T_I = 45$ K,[1] $T_{Br} = 34$ K[3] and $T_{Cl} = 17$ K[5] and the magnetization easy axis is normal to the plane for CrI_3 and $CrBr_3$ while it is in plane for $CrCl_3$.

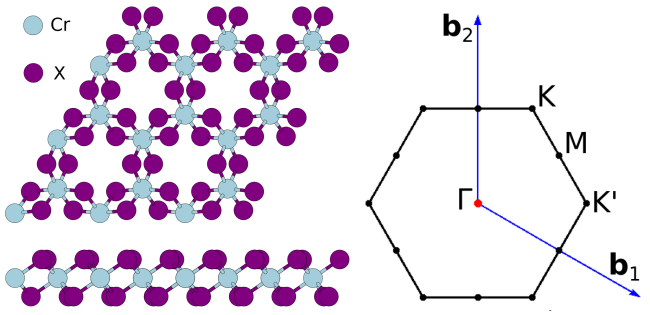

Figure 1. Left: Ball-and-stick model of the crystal structure of monolayer chromium trihalides CrX_3 (X=Cl, Br, I). Right: Brillouin zone of the corresponding hexagonal lattice with the high-symmetry points indicated. $\mathbf{b}_1$ and $\mathbf{b}_2$ denote reciprocal lattice vectors.

Recent Density Functional Theory (LDA) calculations[26–28] confirm the qualitative understandings derived from the ionic model. However, at quantitative level details start to differ from the fully ionic picture; one important such factor is the degree of hybridization of

the t_{2g} levels with the p bands of the ligands. This degree of hybridization depends on the ligand, its atomic weight and the number of core levels, which turns out to be a crucially important factor in determining the detailed electronic band structure. This is the main focus of the present paper which we carefully analyze on different levels of theory beyond conventional density functional theory. Our self-consistent GW (QSGW) and BSE (QS$G\widehat{W}$) implementations are independent of the starting point and, hence, allow us to study the roles of self-consistent charge densities and self-energies in determining the key features of the electronic structures at different levels of the theory. Within our fully self-consistent diagrammatic many-body perturbative first-principles approach the electronic eigenfunctions keep changing with additional diagrams and across the three different materials, depending on the nature of the ligand.

Molecular Picture

Within the local-density approximation (LDA), we find the spin-polarized bandgaps of the three systems to be, 1.51 eV, 1.30 eV and 1.20 eV for X=(Cl, Br, I) respectively, in line with prior work.[26] The qualitative trend is easily understood in terms of the splitting between Cr d and X p atomic levels. In the simplest two-level tight-binding description, the conduction and valence levels are given by $(\varepsilon_d+\varepsilon_p)/2\pm\sqrt{((\varepsilon_d-\varepsilon_p)/2)^2+v^2}$, where ε_d and ε_p are respectively the Cr t_{2g} d and X p atomic levels and v the hybridization matrix element. This results in a gap $E_g=\varepsilon_d-\varepsilon_p+2v^2/(\varepsilon_d-\varepsilon_p)$ to the lowest order in $v/(\varepsilon_d-\varepsilon_p)$. Among all three halides Iodine has the most core levels resulting in its p levels having the most nodes which thus sense the attractive nucleus most weakly. It has the shallowest ε_p of the three halogens, while Cl has the deepest. Thus, the qualitative trend in the bandgap is simply understood as following from the hallide ε_p energies relative to the Cr ε_d. As a slight elaboration on this picture that includes magnetism, we can distinguish between the majority ($t_{2g}^{\uparrow}$) and minority ($t_{2g}^{\downarrow}$) Cr d levels. For the bandgap, the picture just sketched corresponds to the $(\varepsilon_d^{\downarrow}-\epsilon_p)$ bond. A similar picture applies to the $\varepsilon_d^{\uparrow}-\epsilon_p$ bond, but in this channel both bond and antibond are occupied, and moreover $\varepsilon_d^{\uparrow}-\epsilon_p$ need not be large in comparison to v. Indeed the Cr $t_{2g}^{\uparrow}$ and X p levels may overlap.

Energy band picture

The molecular picture qualitatively explains the trends in the bandgap and the admixture of X p in the highest valence states in the sequence ClBrI. However, in the 2D crystal, the molecular levels broaden into bands which can alter the trends in both the bandgap and the merging of X p with Cr $t_{2g}^{\uparrow}$ in the valence bands. The corresponding orbital resolved density of states are shown in Fig. 2. The X p level becomes more shallow, and the highest lying valence band acquires increasing anion character as

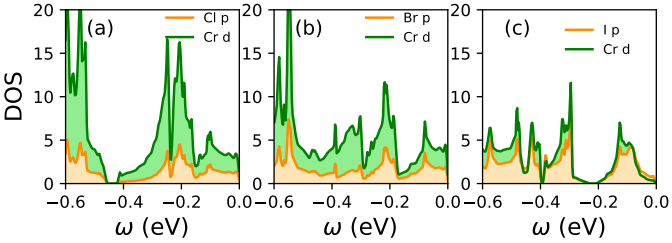

Figure 2. Partial Density of states within the LDA, projected onto the Cr-d and X-p states for (a) X=Cl, (b) Br and (c) I.

theory	ml-bandgap (eV)			ml-spectral weight			bulk bandgap (eV)		
	$CrCl_3$	$CrBr_3$	CrI_3	$CrCl_3$	$CrBr_3$	CrI_3	$CrCl_3$	$CrBr_3$	CrI_3
LDA	1.51	1.30	1.06	21%	26%	42%	1.38	1.2	0.91
QSGW	6.87	5.73	3.25	40%	63%	81%	5.4	4.38	3.0
QS$G\widehat{W}$	5.55	4.65	2.9	24%	31%	64%	4.4	3.5	2.5

Table I. One particle electronic band gap at different levels of theory (with spin-orbit coupling) for both bulk and monolayer variants. The gap increases from LDA to QSGW level. When when ladder diagrams are added two-particle interactions via a BSE, $W\rightarrow\widehat{W}$ and screening is increased. This reduces the QSGW bandgap. Right columns show fraction of spectral weight that the Halogen contributes to the total DOS within an energy window of occupied states $(-0.6,0)$ eV, relative to the valence band maximum. Bulk QS$G\widehat{W}$ bandgaps are 20-25% smaller compared to their monolayer variants.

can be seen both in Table I and in Fig. 2. Spin-orbit coupling only slightly modifies the electronic structure for $CrCl_3$ and $CrBr_3$, while for CrI_3 the bandgap reduces by 150 meV to 1.06 eV in the LDA.

However, as is typical of the LDA, the bandgaps are underestimated, and for CrX_3 the underestimation is severe. Accordingly, we study the electronic structure at three different levels of theory: the LDA, the Quasiparticle Self-Consistent GW approximation (QSGW) ,[29,30] and an extension of QSGW where the RPA approximation to the polarizability is extended by adding ladder diagrams (QS$G\widehat{W}$).[31,32] The electronic dispersions and corresponding DOS are shown in Figs. 3,4,5, for each level of theory and each material. In contrast to typical sp semiconductors, not only the bandgaps but also the valence band dispersions significantly change as the level of theory increases.

QSGW dramatically enhances the gaps relative to the LDA, as is standard in polar compounds.[29] Nevertheless, within the random phase approximation (RPA), it has long been known that W is universally too large,[33,34] and this is reflected in an underestimate of the static dielectric constant ϵ_∞. Empirically, ϵ_∞ seems to be underestimated in QSGW by a nearly universal factor of 0.8, for a wide range of insulators.[35,36] Roughly speaking, at low energy W is universally too large by a factor $1/0.8$[37] and as a result, QSGW bandgaps are slightly overestimated.[29] This can be corrected by extending the RPA

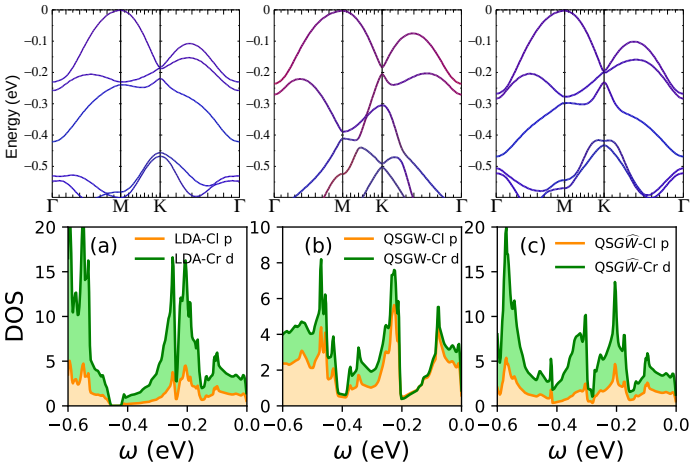

Figure 3. $CrCl_3$: From left to right: LDA, QSGW and QS$G\widehat{W}$ valence band structures (with spin-orbit coupling) are shown respectively. The colors correspond to Cl-p_x+p_y (red), Cl-p_z (green), Cr-d (blue). In the bottom panels are shown the density of states projected onto the Cr-d and Cl-p states at different levels of the theory.

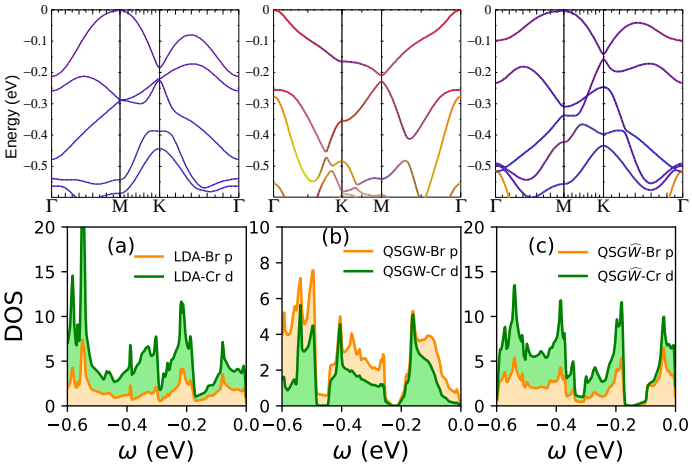

Figure 4. $CrBr_3$: From left to right: LDA, QSGW and QS$G\widehat{W}$ valence band structures (with spin-orbit coupling) are shown respectively. The colors correspond to Br-p_x+p_y (red), Br-p_z (green), Cr-d (blue). In the bottom panels are shown the density of states projected onto the Cr-d and Br-p states at different levels of the theory. Structure of the top most valence band is similar within LDA and QS$G\widehat{W}$, but is different in QSGW. the QS$G\widehat{W}$ top most valence band is much narrower in comparison to both QS$G\widehat{W}$ and LDA and is split from the rest of the valence band manifold.

to introduce an electron-hole attraction in virtual excitations. These extra (ladder) diagrams are solved by a BSE, and they significantly improve on the optics, largely eliminating the discrepancy in ϵ_∞.[31] When ladders are also added to improve W in the GW cycle ($W \rightarrow \widehat{W}$), it significantly improves the one-particle gap as well, as will be discussed elsewhere.[32] This scenario is played out in CrX_3 compounds: QSGW bandgaps are slightly larger than QS$G\widehat{W}$ bandgaps, as seen in Table I. We note that the QS$G\widehat{W}$ band gaps for the bulk variants come out ∼20-25% smaller (see Table I) compared to their monolayer counterparts due to enhanced screening in the bulk, nevertheless, their involved band structural details remain similar.

Remarkably, the structure of the valence band is very sensitive to the level of theory used, which applies to both, the band energies and wave functions. Just for $CrCl_3$ the valence band maximum is independent of the theory and is consistently pinned to the M point (Fig. 3). In the sequence ClBrI, there is an overall tendency for the valence band maximum to shift from the M point to the Γ point. In the LDA this transition occurs after Br and I, while in QSGW the valence band at Γ is above M already for Br. QS$G\widehat{W}$ shows the same tendency as QSGW, but the change is less pronounced and the transition takes place between Br and I. This is a reflection of the softening effects of the ladder diagrams on W.

Structure of valence bands: To understand this curious renormalization of valence bands between different levels of the theory, we perform a series of parametric studies. The key point is the dramatic renormalization in the valence band structure between QSGW and QS$G\widehat{W}$ for $CrBr_3$ and CrI_3. For $CrBr_3$ the valence band maximum is at M in QS$G\widehat{W}$ and at Γ in QSGW. Also the Br-p content is significantly enhanced in the valence bands in QSGW as can be seen in Fig. 4 (b), compared to QS$G\widehat{W}$ (see Fig. 4 (c) and Table I). We perform QS$G\widehat{W}$ calculations by a) applying volume conserving strains (ϵ) along (001), b) shifting the centre of mass of Cr-d up by 0.1 Ry (Cr $+0.1Ry$), c) shifting the centre of mass of Cr-d down by 0.1 Ry (Cr $-0.1Ry$), d) applying U=1 eV on the Cr-d (Cr $U = 1eV$). We see that the valence band structure does not have any dramatic qualitative change (see Fig. 6 (b)) in case of Cr $+0.1Ry$. By shifting the Cr-d band centre up by 0.1 Ry, we effectively reduce the hybridization between Cr-d and X-p moderately. This can be observed in the color projection for the top most valence band as it becomes more blue (Cr-d orbitals) compared to Fig. 6 (a) which has significant red component (Br-p). However, the reverse, Cr $-0.1Ry$ hybridizes more the Cr-d and Br-p and the valence band (see Fig. 6 (c)) starts looking more similar to QSGW results (see Fig. 6 (f)). A similar situation emerges when tensile strain ϵ=7% is applied (see Fig. 6 (d)). However, we derive the most understanding when we U=1 eV is applied on the Cr-d. Applying U shifts the Cr majority spin down and the minority spin up. The gap widens, becomes 5.10 eV compared to 4.65 eV without U, but at the same time increases hybridization with the Br-p. The valence band structure (see Fig. 6 (e)) looks almost entirely similar to the one from QSGW. In short, the self-consistent eigenfunctions from QS$G\widehat{W}$+U is identical with QSGW. This

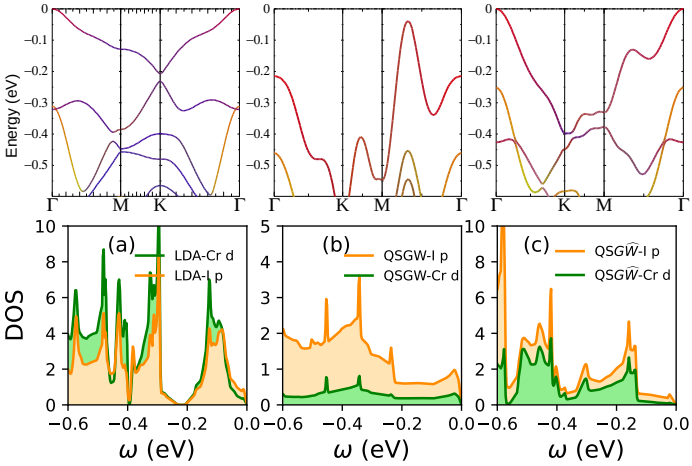

Figure 5. CrI_3 : From left to right: LDA, QSGW and QS$G\widehat{W}$ valence band structures (with spin-orbit coupling) are shown respectively. The colors correspond to I-$p_x + p_y$ (red), I-p_z (green), Cr-d (blue). In the bottom panels are shown the density of states projected onto the Cr-d and I-p states at different levels of the theory. Note that in the QSGW case, the valence band maximum is at a low-symmetry point not on the lines of the figure.

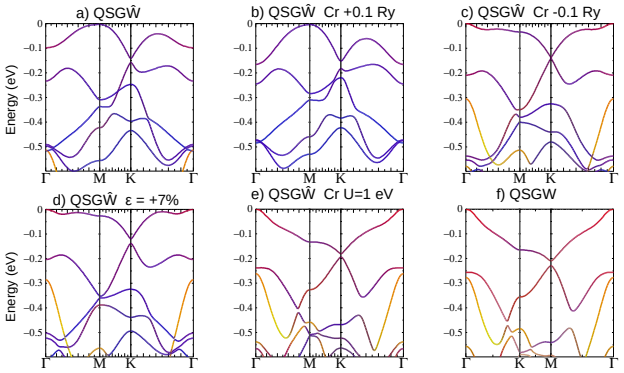

Figure 6. $CrBr_3$: QS$G\widehat{W}$ valence band structures (with spin-orbit coupling) are shown under different perturbations. Weak perturbations can modify the Cr-d and Br-p hybridization and qualitatively modify the valence band structure. a) and f) are the unperturbed QS$G\widehat{W}$ and QSGW valence band structures, b) Cr $+0.1Ry$ is the QS$G\widehat{W}$ solution after shifting the Cr-d band centre up by 0.1 Ry, c) Cr $-0.1Ry$ is the QS$G\widehat{W}$ solution after shifting the Cr-d band centre down by 0.1 Ry, d) ϵ=7% is QS$G\widehat{W}$ solution with 7% volume conserving strain along (001). e) QS$G\widehat{W}$+U solution with U=1 eV on the Cr-d. The colors correspond to I-$p_x + p_y$ (red), I-p_z (green), Cr-d (blue).

also establishes the fact that, albeit their apparent dissimilarities, the QS$G\widehat{W}$ and QSGW solutions are quite similar and it is possible to flip between the two by applying weak perturbations. This is intriguing as it implies that it would also be possible to dramatically alter the valence band structures of CrX_3 in real world experiments with weak perturbations. We observe that the situation is similar in bulk as well, where for $CrBr_3$ and CrI_3 the valence band structure is qualitatively different between QSGW and QS$G\widehat{W}$. Altogether they suggest that the source of this observation lies in the details of the W and not in the dimensionality of the materials. The fact that the QS$G\widehat{W}$ and QSGW are identical for X=Cl and most different in X=I, can now naturally be understood. In X=I, the I-p states are the shallowest compared to the Cr-d states and, hence, to change the valence band manifold by tweaking Cr-d and I-p hybridization is easy in CrI_3, while it's most difficult in $CrCl_3$.

Recent works implementing single-shot GW, with approximations different from QSGW, also finds the valence band maximum in CrI_3 at Γ,[26,38] which also seems to be confirmed by a recent ARPES study.[39] Two recent theoretical works report one-particle band-gaps of 2.23 eV and 1.57 eV respectively, from QSGW[40] and QSGW+BSE.[41] Lee et el.[40] uses a manually scaled QSGW Σ to produce the gap of 2.23 eV. Note that their estimate for band gap is very similar to our bulk estimate of 2.5 eV and smaller than our monolayer estimate of 2.9 eV. Presumably their valence band structure from QSGW is different from ours, because of the manual scaling of Σ. For CrI_3 Kutepov[41] includes vertex corrections both in W and Σ to produce the gap of 1.57 eV. This is a significant difference from our QS$G\widehat{W}$ implementation and we can expect the results to be different. Also as we discuss above in cases with Cr $-0.1Ry$ and ϵ=7%, the electronic gap reduces in both cases. One can expect this to be qualitatively the direction where the band gap approaches as the vertex is explicitly incorporated in Σ, in the spirit of the smaller band gap that Kutepov find from his implementation. However, it is not clear from these works[40,41] whether the vacuum corrections were incorporated or not. Vacuum corrections in our method lead to enhancement in band gap by ∼0.3-0.4 eV. Hence, a rigorous comparison of the absolute value of the band-gap against our findings is difficult. In another work, Wu et al.[42] achieves one-particle band gap of 3.8 eV in G_0W_0 in $CrBr_3$. They use a LSDA+U starting mean-field potential with choices of U=1.5 eV and J=0.5 eV for their one-shot G_0W_0. G_0W_0 only updates the LSDA+U eigenvalues but does not change the eigenfunctions. Also our implementation being fully self-consistent and starting-point-independent, we don't have any free parameters like U and/or J. In a separate work, Molina et al.[26] employs G_0W_0 with LSDA+U starting parameters that are completely consistent with the work by Wu et al..[42] However, Molina et al. achieves a band gap of 4.45 eV for $CrBr_3$. G_0W_0 is known to produce smaller band gaps compared to QSGW. QSGW systematically produces larger band gaps since W gets under-screened via self-consistency, which is corrected as ladder diagrams are incorporated in W. This we can see as our estimate for

theory	$CrCl_3$		$CrBr_3$		CrI_3	
	m_x	m_y	m_x	m_y	m_x	m_y
LDA	1.9	3.6	2.0	5.2	1.2	1.2
QSGW	2.3	5.5	∞	-1.3	1.4	1.4
QS$G\widehat{W}$	2.1	4.2	3.2	∞	0.57	0.57

Table II. Effective masses m^*/m_0 at the M point (as shown in Fig. 1) for $CrCl_3$ and $CrBr_3$, and at the Γ point for CrI_3, for three levels of approximation. These k points correspond to the valence band maximum except for $CrBr_3$ in the QSGW approximation (see Fig. 5). m_x and m_y correspond to orientations perpendicular and parallel to the Γ-M line, respectively. ∞ is a shorthand for an effective mass larger than $10m_0$.

QS$G\widehat{W}$ band gap of 4.65 eV is more closer to the G_0W_0 estimate of 4.45 eV by Molina et al. Note that in bulk variants, we achieve band gaps which are $\sim 20\%$ smaller in all cases compared to their monolayer variants. Again in both the works from Wu et al. and Molina et al. we don't find any comments on the vacuum corrections. In $CrBr_3$, in absence of the vacuum corrections, we achieve a gap of 4.26 eV from our QS$G\widehat{W}$ implementation which is much closer to the estimates from the works that uses G_0W_0.

To further understand these remarkable changes in the valence band structures, we analyse the electronic eigenfunctions from different levels of the theory. Even though the QS$G\widehat{W}$ band structure more closely resembles LDA than QSGW, the eigenfunctions do not. This can be seen by inspecting the square of the wave function, $|\psi|^2$, corresponding to the highest-lying state at the M point (Fig. 7 The density is plotted in real space, and the abscissa and ordinate are defined by the the inverse transpose of the 2×2 matrix composed of $\mathbf{b_1}$ and $\mathbf{b_2}$ of Fig. 1. Throughout this paper x and y are defined by aligning $\mathbf{b_2}$ parallel to y. In this notation the M point is on the $\mathbf{b_2}$ line, or the y axis. Contour plots in two planes are shown, passing through Cr and Br, respectively. At the LDA level (top panels), the wave function resembles an atomic d_{xy} state centered at each Cr nucleus. In the Br plane some Br p character is evident, and the bond is partially directed along x. The middle panels depict the change in $|\psi|^2$ when passing from LDA to QSGW. Two effects are prominent: first there is a transfer of spectral weight from Cr to Br (mostly green contours on Cr, red on Br) as also noted in Table I. Second, the bonding becomes more directional, forming one-dimensional chains along x. This reflects an enhancement of the Cr-Cr coupling mediated through the Br. It is especially apparent in the Br plane, but it is also reflected in the asymmetry between the x and y directions in the Cr plane. The bottom two panels show the change in $|\psi|^2$ when passing from QSGW to QS$G\widehat{W}$. QS$G\widehat{W}$ seems to undo some effect of QSGW, although the changes remain moderate. This suggests that the QSGW and QS$G\widehat{W}$ eigenfunctions are not significantly different.

The directionality in the wave function is also reflected in strong anisotropy in the valence band mass at the point M, particularly in $CrBr_3$ (see Table. II). By symmetry, there is no anisotropy at the Γ point, but at M it becomes quite pronounced at the highest level of theory.

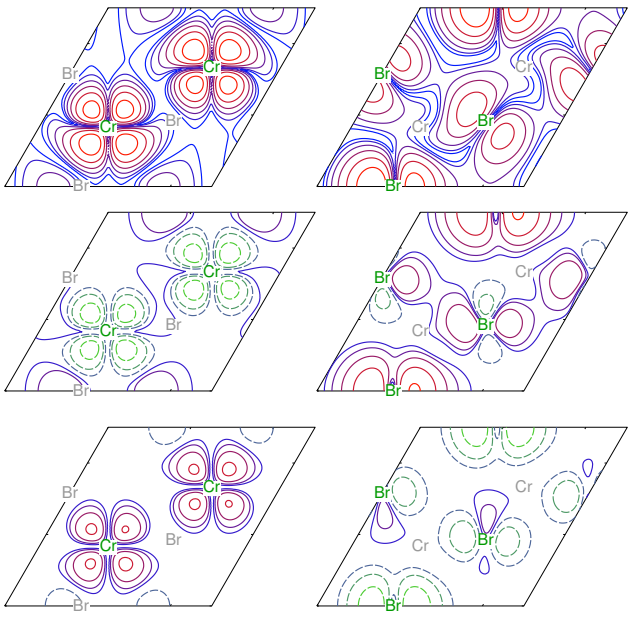

Figure 7. $CrBr_3$: Square of wave function ψ, in real space, of the highest valence band state at the M point. All the left panels pass through a Cr plane and right panels pass through a Br plane. Cr and Br site positions are labelled in green in the plane where the reside, and gray when they lie in a different plane. Top panels display constant-amplitude contours for LDA eigenfunctions. Contours are taken in half-decade increments in $|\psi|^2$, with a factor of 300 between highest contour (red) and lowest (blue). In the Cr plane, the atomic d_{xy} character centered at Cr nuclei stand in sharp relief; in the Br plane the Br atomic p character is evident. Middle panels show the change in $|\psi|^2$ passing from LDA to QSGW eigenfunctions; bottom panels show the corresponding change passing from QSGW to QS$G\widehat{W}$ eigenfunctions. In the bottom four panels, bluered has a similar meaning as in the top panels (increasing positive $\delta|\psi|^2$), while contours of negative $\delta|\psi|^2$ are depicted by increasing strength in the change blue-green. Note that the color patterns in the middle panels and bottom panels are mirror images. As a consequence of the softening in W in the change $W \to \widehat{W}$, the shift in density LDA→QSGW is partially reversed by the addition of ladder diagrams.

Finally, we analyze the dynamic and momentum dependent self energies $\Sigma(k,\omega)$ from QSGW and QS$G\widehat{W}$ to further understand the changes in the valence band structure at different levels of theory. We observe that the Σ of the top most valence band has very week dependence on momentum. The momentum dependence is even weaker in the down spin channel, that is unoccupied. For the up spin channel the momentum dispersion is very similar both in QSGW and QS$G\widehat{W}$. We extract the quasi-particle renormalization (Z_k) factors from

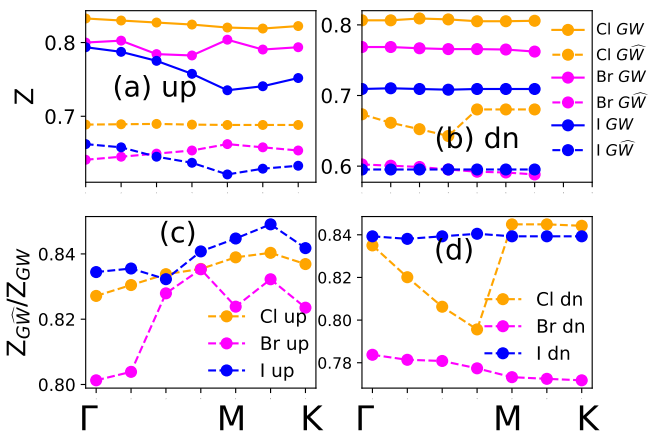

Figure 8. CrX_3 : Real part of $\Sigma(k,\omega)$ is analyzed to extract the quasi-particle renormalization factor Z_k from QSGW and QS$G\widehat{W}$. (a) and (b) show the weak momentum dependence of the Z_k for the top most valence band at the quasi-particle peaks at the k points chose along the high symmetry directions of the first Brillouin zone for the up and down spin sectors respectively. (c) and (d) show the relative suppression of the Z_k factor in QS$G\widehat{W}$, compared to QSGW for the up and down spin sectors respectively.

$\Sigma(k,\omega)$ at the quasi-particle energies for the top most valence band. We observe that Z_k reduces by ∼20% within QS$G\widehat{W}$ in comparison to QSGW. This suggests that the quasi-particles become further localized at the QS$G\widehat{W}$ level, in comparison to the QSGW. This goes along with charge density that is weakly put back on the atoms at the QS$G\widehat{W}$ level.

Conclusions

We analyze in detail the electronic band structure of CrX_3 within different levels of an *ab initio* theory. The results were interpreted in terms of a simplified tight-binding model to elucidate the trends in ClBrI, in particular the bandgap and the orbital character of the valence band. Many-body effects both enhance the bandgap, and make the valence band eigenfunctions more directional. We also showed that addition of ladder diagrams to improve W increases the screening, thus softening the many body corrections to LDA. Further we quantify the momentum dependence of the self-energies at different levels of the theory and show explicitly how excitonic correlations lead to re-normalization of the electronic bands and localization of charges. As the hybridization between Cr-d and X-p enhances in the direction ClBrI, the systems become more 'band-like' with lesser electronic correlations. In the same sequence, as the X-p states become shallower with respect to the Cr-d states, we show explicitly that weak perturbations can significantly modify the hybridization and thereby leading to qualitative changes in the valence band features. Summarily, we show how a starting point independent implementation of GW and *BSE* leads to changes in electronic band energies and wavefunctions via complicated interplay between charge and self-energy self-consistencies in CrX_3.

Acknowledgment

MIK, ANR and SA are supported by the ERC Synery Grant, project 854843 FASTCORR (Ultrafast dynamics of correlated electrons in solids). MvS and DP are supported by the Simons Many-Electron Collaboration. We acknowledge PRACE for awarding us access to Irene-Rome hosted by TGCC, France and Juwels Booster and Clusters, Germany; STFC Scientific Computing Department's SCARF cluster, Cambridge Tier-2 system operated by the University of Cambridge Research Computing Service (www.hpc.cam.ac.uk) funded by EPSRC Tier-2 capital grant EP/P020259/1.

Appendix A: Numerical Details

Single particle calculations (LDA, and energy band calculations with the static quasiparticlized QSGW self-energy $\Sigma^0(k)$) were performed on a 16×16×1 k-mesh while the (relatively smooth) dynamical self-energy $\Sigma(k)$ was constructed using a 6×6×1 k-mesh and Σ^0(k) extracted from it. For each iteration in the QSGW self-consistency cycle, the charge density was made self-consistent. The QSGW cycle was iterated until the RMS change in Σ^0 reached 10^{-5} Ry. Thus the calculation was self-consistent in both $\Sigma^0(k)$ and the density. Numerous checks were made to verify that the self-consistent $\Sigma^0(k)$ was independent of starting point, for both QSGW and QS$G\widehat{W}$ calculations; e.g. using LDA or Hartee-Fock self-energy as the initial self energy for QSGW and using LDA or QSGW as the initial self-energy for QS$G\widehat{W}$.

For the present work, the electron-hole two-particle correlations are incorporated within a self-consistent ladder-BSE implementation[31,32] with Tamm-Dancoff approximation.[43,44] The effective interaction W is calculated with ladder-BSE corrections and the self energy, using a static vertex in the BSE. G and W are updated iteratively until all of them converge and this is what we call QS$G\widehat{W}$. Ladders increase the screening of W, reducing the gap besides softening the LDAQSGW corrections noted for the valence bands.

For all materials, we checked the convergence in the QS$G\widehat{W}$ band gap by increasing the size of the two-particle Hamiltonian. We increase the number of valence and conduction states that are included in the two-particle Hamiltonian. We observe that for all materials the QS$G\widehat{W}$ band gap stops changing once 24 valence and 24 conduction states are included in the two-particle Hamiltonian. While the gap is most sensitive to the number of valence states, 14 conducting states produces re-

variants	$CrCl_3$	$CrBr_3$	CrI_3
LDA	4.23	4.44	4.66
QSGW	4.08	4.3	4.66
BSE	4.11	4.35	4.64

Table III. Shown are the Cr-d occupancies.

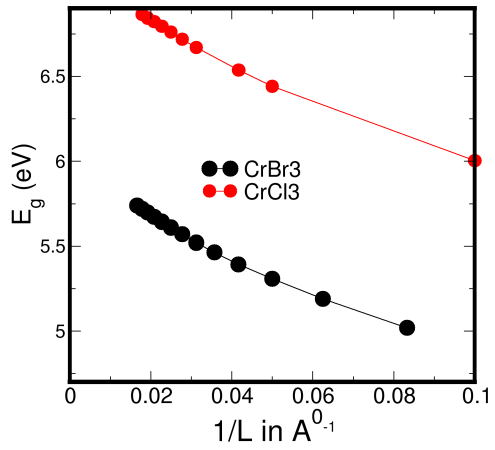

Figure 9. $CrBr_3$ and $CrCl_3$: Scaling of the one particle band gap from QSGW with vacuum size L.

sults within 2% error of the converged results from 24 conduction states.

In Tab. III we list the Cr-d occupancies for different materials at different levels of the theory.

Appendix B: Vacuum Distance Scaling

Periodic boundary conditions were used in all directions, introducing an unwanted coupling between $CrBr_3$ slabs. To minimize this coupling a vacuum of length L was inserted between slabs, and L was varied.

As is well known, the QSGW is known to fix the infamous 'gap problem'[45] in insulators, we observe that the band gap increases significantly in all three compounds within QSGW; 6.87 eV in Cl, 5.73 eV in Br and 3.25 eV in I (see I). We change the vacuum length from 10 Å to 80 Å, and observe the scaling of the band gap with vacuum size (L). We observe an almost perfect 1/L scaling (see Fig. 9) of the gap as noted earlier in a separate work on V_2O_5 .[46] This also allows us to check the dielectric constant (ϵ_∞) and its vacuum correction. In the limit of a purely free standing monolayer all three directional components of the macroscopic dielectric response in the static limit approaches 1, suggesting the absence of screening. We use this vacuum length (60 Å) for the rest of the discussions in the present work.

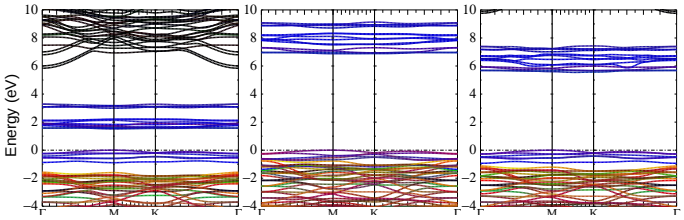

Figure 10. $CrCl_3$: The colors correspond to Cl-$p_x + p_y$ (red), Cl p_z (green), Cr-d (blue) (From left to right: LDA, QSGW and QS$G\widehat{W}$ respectively).

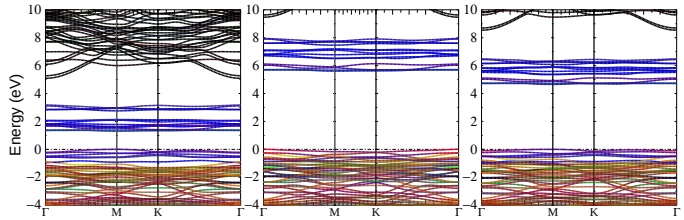

Figure 11. $CrBr_3$: The colors correspond to Br-$p_x + p_y$ (red), Br p_z (green), Cr-d (blue) (From left to right: LDA, QSGW and QS$G\widehat{W}$ respectively).

Appendix C: Full Band Structures

In Fig. 10, Fig. 11, Fig. 12 we show the band structures for all materials over larger energy windows.

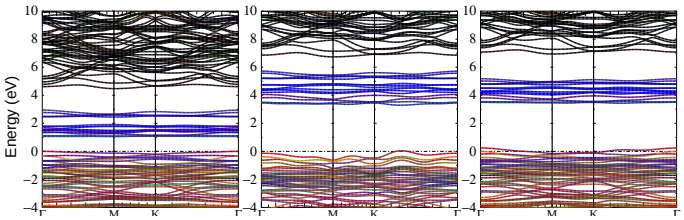

Figure 12. CrI_3 : The colors correspond to I-$p_x + p_y$ (red), I p_z (green), Cr-d (blue) (From left to right: LDA, QSGW and QS$G\widehat{W}$ respectively).

* swagata.acharya@ru.nl

[1] B. Huang, G. Clark, E. Navarro-Moratalla, D. R. Klein, R. Cheng, K. L. Seyler, D. Zhong, E. Schmidgall, M. A. McGuire, D. H. Cobden, *et al.*, Nature **546**, 270 (2017).

[2] D. R. Klein, D. MacNeill, J. L. Lado, D. Soriano, E. Navarro-Moratalla, K. Watanabe, T. Taniguchi, S. Manni, P. Canfield, J. Fernández-Rossier, *et al.*, Science **360**, 1218 (2018).

[3] Z. Zhang, J. Shang, C. Jiang, A. Rasmita, W. Gao, and T. Yu, Nano letters **19**, 3138 (2019).

[4] M. Kim, P. Kumaravadivel, J. Birkbeck, W. Kuang, S. G. Xu, D. Hopkinson, J. Knolle, P. A. McClarty, A. Berdyugin, M. B. Shalom, *et al.*, Nature Electronics **2**, 457 (2019).

[5] X. Cai, T. Song, N. P. Wilson, G. Clark, M. He, X. Zhang, T. Taniguchi, K. Watanabe, W. Yao, D. Xiao, *et al.*, Nano letters **19**, 3993 (2019).

[6] C. Gong, L. Li, Z. Li, H. Ji, A. Stern, Y. Xia, T. Cao, W. Bao, C. Wang, Y. Wang, *et al.*, Nature **546**, 265 (2017).

[7] Z. Fei, B. Huang, P. Malinowski, W. Wang, T. Song, J. Sanchez, W. Yao, D. Xiao, X. Zhu, A. F. May, *et al.*, Nature materials **17**, 778 (2018).

[8] Y. Deng, Y. Yu, M. Z. Shi, Z. Guo, Z. Xu, J. Wang, X. H. Chen, and Y. Zhang, Science **367**, 895 (2020).

[9] C. Gong and X. Zhang, Science **363** (2019).

[10] M. Gibertini, M. Koperski, A. Morpurgo, and K. Novoselov, Nature nanotechnology **14**, 408 (2019).

[11] N. D. Mermin and H. Wagner, Physical Review Letters **17**, 1133 (1966).

[12] V. Y. Irkhin, A. Katanin, and M. Katsnelson, Physical Review B **60**, 1082 (1999).

[13] D. Soriano, M. I. Katsnelson, and J. Fernández-Rossier, Nano Letters **20**, 6225 (2020).

[14] S. Jiang, L. Li, Z. Wang, K. F. Mak, and J. Shan, Nature nanotechnology **13**, 549 (2018).

[15] S. Jiang, J. Shan, and K. F. Mak, Nature materials **17**, 406 (2018).

[16] Z. Wang, T. Zhang, M. Ding, B. Dong, Y. Li, M. Chen, X. Li, J. Huang, H. Wang, X. Zhao, *et al.*, Nature nanotechnology **13**, 554 (2018).

[17] M. Bonilla, S. Kolekar, Y. Ma, H. C. Diaz, V. Kalappattil, R. Das, T. Eggers, H. R. Gutierrez, M.-H. Phan, and M. Batzill, Nature nanotechnology **13**, 289 (2018).

[18] S. Jiang, L. Li, Z. Wang, J. Shan, and K. F. Mak, arXiv preprint arXiv:1807.04898 (2018).

[19] T. Song, X. Cai, M. W.-Y. Tu, X. Zhang, B. Huang, N. P. Wilson, K. L. Seyler, L. Zhu, T. Taniguchi, K. Watanabe, *et al.*, Science **360**, 1214 (2018).

[20] T. Song, M. W.-Y. Tu, C. Carnahan, X. Cai, T. Taniguchi, K. Watanabe, M. A. McGuire, D. H. Cobden, D. Xiao, W. Yao, *et al.*, Nano letters **19**, 915 (2019).

[21] Z. Wang, I. Gutiérrez-Lezama, N. Ubrig, M. Kroner, M. Gibertini, T. Taniguchi, K. Watanabe, A. Imamoğlu, E. Giannini, and A. F. Morpurgo, Nature Communications **9**, 2516 (2018).

[22] H. H. Kim, B. Yang, T. Patel, F. Sfigakis, C. Li, S. Tian, H. Lei, and A. W. Tsen, Nano letters **18**, 4885 (2018).

[23] I. Kashin, V. Mazurenko, M. Katsnelson, and A. Rudenko, 2D Materials **7**, 025036 (2020).

[24] Y. Kvashnin, A. Bergman, A. Lichtenstein, and M. Katsnelson, Physical Review B **102**, 115162 (2020).

[25] D. Soriano, A. N. Rudenko, M. I. Katsnelson, and M. Rösner, "Environmental screening and ligand-field effects to magnetism in cri_3 monolayer," (2021), arXiv:2103.04686 [cond-mat.str-el].

[26] A. Molina-Sanchez, G. Catarina, D. Sangalli, and J. Fernandez-Rossier, Journal of Materials Chemistry C **8**, 8856 (2020).

[27] S. V. Streltsov and D. I. Khomskii, Physics-Uspekhi **60**, 1121 (2017).

[28] D. Soriano, C. Cardoso, and J. Fernández-Rossier, Solid State Communications **299**, 113662 (2019).

[29] M. van Schilfgaarde, T. Kotani, and S. Faleev, Physical review letters **96**, 226402 (2006).

[30] D. Pashov, S. Acharya, W. R. Lambrecht, J. Jackson, K. D. Belashchenko, A. Chantis, F. Jamet, and M. van Schilfgaarde, Computer Physics Communications **249**, 107065 (2020).

[31] B. Cunningham, M. Grüning, P. Azarhoosh, D. Pashov, and M. van Schilfgaarde, Physical Review Materials **2**, 034603 (2018).

[32] B. Cunningham, M. Gruening, D. Pashov, and M. van Schilfgaarde, "Qsgw: Quasiparticle self consistent gw with ladder diagrams in w," (2021), arXiv:2106.05759 [cond-mat.mtrl-sci].

[33] S. Albrecht, L. Reining, R. Del Sole, and G. Onida, Physical review letters **80**, 4510 (1998).

[34] M. Rohlfing and S. G. Louie, Physical Review B **62**, 4927 (2000).

[35] A. N. Chantis, M. van Schilfgaarde, and T. Kotani, Physical review letters **96**, 086405 (2006).

[36] C. Bhandari, M. van Schilgaarde, T. Kotani, and W. R. Lambrecht, Physical Review Materials **2**, 013807 (2018).

[37] D. Deguchi, K. Sato, H. Kino, and T. Kotani, Japanese Journal of Applied Physics **55**, 051201 (2016).

[38] M. Wu, Z. Li, T. Cao, and S. G. Louie, Nature Communications **10**, 2371 (2019).

[39] A. Kundu, Y. Liu, C. Petrovic, and T. Valla, Scientific Reports **10**, 15602 (2020).

[40] Y. Lee, T. Kotani, and L. Ke, Phys. Rev. B **101**, 241409 (2020).

[41] A. L. Kutepov, "Electronic structure of van der waals ferromagnet cri_3 from self consistent vertex corrected gw approaches," (2021), arXiv:2105.07798 [cond-mat.mtrl-sci].

[42] M. Wu, Z. Li, and S. G. Louie, "Optical and magneto-optical properties of ferromagnetic monolayer $crbr_3$: A first-principles *gw* and *gw* plus bethe-salpeter equation study," (2021), arXiv:2106.00770 [cond-mat.mtrl-sci].

[43] S. Hirata and M. Head-Gordon, Chemical Physics Letters **314**, 291 (1999).

[44] G. Myrta, A. Marini, and X. Gonze, Nano Letters **9**, 2820 (2009).

[45] F. Aryasetiawan and O. Gunnarsson, Reports on Progress in Physics **61**, 237 (1998).

[46] C. Bhandari, W. R. Lambrecht, and M. van Schilfgaarde, Physical Review B **91**, 125116 (2015).